Geophysical Prospecting, 2007, **55**, 655–669

Attenuation tomography: An application to gas-hydrate and free-gas detection

Giuliana Rossi*, Davide Gei, Gualtiero Böhm, Gianni Madrussani and José M. Carcione

Department of Geophysics, Istituto Nazionale di Oceanografia e di Geofisica Sperimentale-OGS, Borgo Grotta Gigante 42c, 34010 Sgonico, Trieste, Italy

Received January 2006, revision accepted March 2007

ABSTRACT

We estimate the quality factor (Q) from seismic reflections by using a tomographic inversion algorithm based on the frequency-shift method. The algorithm is verified with a synthetic case and is applied to offshore data, acquired at western Svalbard, to detect the presence of bottom-simulating reflectors (BSR) and gas hydrates. An array of 20 ocean-bottom seismographs has been used.

The combined use of traveltime and attenuation tomography provides a 3D velocity–Q cube, which can be used to map the spatial distribution of the gas-hydrate concentration and free-gas saturation. In general, high P-wave velocity and quality factor indicate the presence of solid hydrates and low P-wave velocity and quality factor correspond to free-gas bearing sediments.

The Q-values vary between 200 and 25, with higher values (150–200) above the BSR and lower values below the BSR (25–40). These results seem to confirm that hydrates cement the grains, and attenuation decreases with increasing hydrate concentration.

INTRODUCTION

Knowledge of rock-physics properties is essential for quantifying the amount of hydrocarbons, geothermal resources, and aquifer contaminants and pollution.

In particular, estimation of the quality factor from seismic data is useful for determining the presence of pore-fluids and pore-fillings, and to quantify saturation, porosity and permeability (e.g. the classical works of Wyllie, Gardner and Gregory 1962, 1963; Gardner, Wyllie and Droshak 1964; and successively Mavko and Nur 1979; Berryman 1988; Carcione, Helle and Pham 2003; Carcione and Picotti 2006). Moreover, it is well known that incorporating the effects of attenuation in the evaluation of the reflection coefficients is essential for a proper amplitude-variations-with-offset (AVO) analysis, since attenuation affects the post-critical reflections substantially (Carcione, Helle and Zhao 1998; Chapman, Liu and Li 2006).

*E-mail: grossi@inogs.it

Attenuation is an important indicator of the state of the rock, since in dry rocks it is one order of magnitude lower than attenuation in saturated samples. Moreover, attenuation is more anisotropic than slowness (inverse of seismic velocity) (e.g. Carcione 2001). Laboratory data on prestressed rocks reveal that attenuation may be more sensitive to the closing of cracks than the elastic stiffnesses. In that case, accurate estimates of wave attenuation can be used to quantify permeability, porosity and stress-induced anisotropy (Best, McCann and Sothcott 1994; Dasgupta and Clark 1998).

The algorithm used to estimate attenuation is based on a relationship between the quality factor and the centroid frequency of the spectrum, which, as in the case of traveltime tomography, is a linear integral along the raypath.

Attenuation tomography, based on seismic amplitude changes, has been attempted for many years (e.g. Brzostowski and McMechan 1992), and recently, interesting results have been achieved for crustal studies (Roth *et al.* 1999) and for shallow studies, both with seismic and with

ground-penetrating-radar data (Quan and Harris 1997; Liu, Lane and Quan 1998). In particular, the approach of Quan and Harris (1997) and Liu *et al.* (1998) uses the pulse broadening that occurs due to the fact that the high-frequency part of the spectrum decreases faster than its low-frequency part as the wave propagates within the earth and is attenuated. This method appears to be more robust with respect to those based on amplitude decay, since amplitudes may be affected by many factors whose effects may be confused with those induced by intrinsic attenuation. In contrast, pulse broadening, or frequency shift, is not affected by far-field geometrical spreading and transmission/reflection losses. The rise-time associated with pulse broadening (Kjartansson 1979; Zucca, Hutchings and Kasameyer 1994) or spectral centroid shift may be used to quantify the frequency shift due to attenuation, the latter being more robust and precise (Quan and Harris 1997; Konofagou *et al.* 1999; Picotti and Carcione 2006). In most of these studies, the Q-factor is assumed to be constant, meaning a linear increase in attenuation with frequency, since the frequency band of seismic experiments is limited. When dealing with data from broader frequency bands, such as surface-wave and earthquake data, this assumption is no longer valid and proper exponential laws have to be taken into account (e.g. van der Baan 2002).

Until now, most applications of attenuation tomography used cross-well data and head waves (Quan and Harris 1997; Plessix 2006). The present work presents an application of the frequency-shift method to 3D seismic reflection tomography. The result of the inversion is therefore integrated information about velocities and attenuation of seismic waves in the different formations of the sediment volume investigated. After testing the method on a synthetic case, we apply it to the tomographic analysis of a 3D real seismic data set, acquired offshore western Svalbard within the framework of the European Union Hydratech project, to detect the presence of gas hydrates and free gas within the sediments on the continental margins and to carry out a quantitative analysis (Westbrook *et al.* 2005; Carcione *et al.* 2005).

THE METHOD

The basis of the tomographic method is the relationship between the recorded traveltime and the seismic velocities of the geological layers, through a line integral along the raypath. The space is discretized in pixels (voxels in 3D), and the integral is replaced by a summation as follows:

$$\Delta t = t^{OBS} - t^{CALC} = \sum_j \Delta s_j \Delta u_j, \tag{1}$$

where t^{OBS} is the observed ray-traveltime, t^{CALC} is the calculated ray-traveltime, Δs_j is the ray segment within the *jth* pixel, and Δu_j is the slowness variation in the *jth* pixel.

As the wave propagates within the earth, it looses the high frequencies, its amplitude decreases and pulse broadening occurs.

A measure of the frequency shift of the spectrum is the spectral content of the pulse, ξ, defined as

$$\xi = (f_S - f_R)/\sigma_S^2, \tag{2}$$

where f_S is the centroid frequency at the source, f_R is the centroid frequency at the receiver, and σ_S^2 is the spectral variance of the pulse (Quan and Harris 1997). For non-Gaussian spectra, Quan and Harris (1997) derived approximate formulae, both for boxcar spectra of bandwidth B,

$$\xi \approx 12(f_S - f_R)/B^2, \tag{2a}$$

and for a triangular spectrum of bandwidth B,

$$\xi \approx 18(f_S - f_R)/B^2, \tag{2b}$$

that are useful when the real spectra are not Gaussian. We tested all of them, and even if the difference is small, we generally adopted the formula (2b) for a triangular spectrum, which gives a better fit to the data analysed here.

A relationship similar to equation (1) can be established between the spectral content and the attenuation, i.e.

$$\Delta\xi = \xi^{OBS} - \xi^{CALC} = \sum_j \Delta s_j \Delta\alpha_{0_j}, \tag{3}$$

where Δs_j is the segment of the ray within one of the pixels and α_0 is the attenuation factor of the rocks; $\alpha_0 = \pi/Qv$, where Q is the quality factor of the medium and v is its velocity. The attenuation factor is related to the attenuation α by the equation, $\alpha = \alpha_0 f$, where f is the frequency. This simplification may be safely used within the frequency range of a seismic experiment (e.g. Kjartansson 1979; Zucca *et al.* 1994; Quan and Harris 1997). From equations (2), (2a) and (2b), it follows that a broader input bandwidth leads to a greater frequency change, and that a broad input frequency band is important for a robust estimation of Q.

The main problem is the estimation of the original amplitude spectrum of the seismic pulse when the source signature is not available. In general, it is assumed that one of the recorded seismic phases is not affected by attenuation, and its spectrum may be used as a reference. For marine surveys, the direct or first arrival may be safely used as a reference, and the frequency changes in the other phases are calculated on this

basis. A preliminary test on the stationarity of the spectrum over the offset range considered is necessary, since at large offsets, refracted arrivals could be the first arrivals: having different raypaths, they can consequently have spectra that are different from the near-offset ones. Furthermore, on land, surface heterogeneities may change the frequency content of the first arrivals laterally, so that we may obtain only a relative variation of the attenuation with respect to the shallowest layer (e.g. Böhm *et al.* 2006).

In order to choose the same seismic phases used for the traveltime tomography, we use the times picked for the velocity inversion as centres of the temporal windows (w1 in Fig. 3a) over which we perform the spectral analysis, both for the reference pulse and for the analyzed phase. A zoom of the two wavelets is shown in Fig. 3(b, c). To minimize possible noise problems, a lateral sliding window of 20–30 traces is also used (*w2* in Fig. 3a), and the resulting averaged spectra (Fig. 3d, e), interpolated with a polynomial, are assigned to the central trace. The fifth-order polynomial interpolation of the amplitude spectra is of importance when noise affects the amplitude spectrum, destroying some frequency bands and so compromising the calculation of the spectral centroid. A least-mean-square fitting is the basis of the calculation of the polynomial coefficients, and the polynomial order is chosen by minimizing the root-mean-square errors. When we use a single reference spectrum for the analysis, *w2* is set to be coincident with the trace number of the data set, or better, to be smaller than the trace number, so as to follow eventual lateral variations of the shallowest layer. In an onshore case with known topographical and geological lateral variations, Böhm *et al.* (2006) estimated the reference power spectrum by averaging the power spectra relative to the nearest first arrivals, (excluding the zero-offset arrivals), and showed the effect of different averaging window widths.

The above-described procedure allows us to use the velocity field with depth, obtained by means of the previously performed traveltime tomographic inversion, for the ray tracing. The same velocity field is also used to convert α to Q.

Hence, at the end of the process, a multiparameter 3D model with depth is obtained. This provides information on both velocity and attenuation for the same seismic events and, therefore, on the rock formations crossed by the rays considered. We use the method described in detail by Vesnaver *et al.* (1999) for both velocity and attenuation inversion. It uses a modified version of the minimum-time ray-tracing method developed by Böhm *et al.* (1999) and an iterative process for the inversion, based on the simultaneous iterative reconstruction technique (SIRT) algorithm (van der Sluis and van der Vorst 1987). SIRT is a robust, although slowly converging method, which is also robust in the presence of noise. It gives a generally smooth velocity field as solution (e.g. Dobroka *et al.* 1992). A useful property of SIRT is the possibility of applying some constraints on the solution, obtained from other kinds of information, such as logs or geological models, although a limitation of SIRT is that it allows larger amplitudes for the solution in poorly visited cells (Spakman and Nolet 1988). It is therefore necessary to minimize the ray-count differences in the pixels, or to evaluate the reliability of the solution for each one of them. A measure of the reliability of the tomographic inversion is the null space energy, based on the singular-value decomposition of the tomographic matrix (e.g. Vesnaver 1994). This is a measure not only of the ray number in each pixel, but also of the independence of the tomographic matrix equations, and therefore of the matrix rank. Null space energy values vary from 0 to 1, where 1 is related to underdetermined matrices, and to an infinite number of solutions that satisfy the system. Thus we may retain the regions of the model where the null space is low and therefore the reliability is high, and not consider the regions where the reliability is poor. The staggered-grids procedure achieves the same results acting on the grid. A coarse grid is chosen, such that the coverage in each cell is similar and high, and small shifts are applied in the *x*- and *y*-directions; the resulting inverted fields are averaged, thus

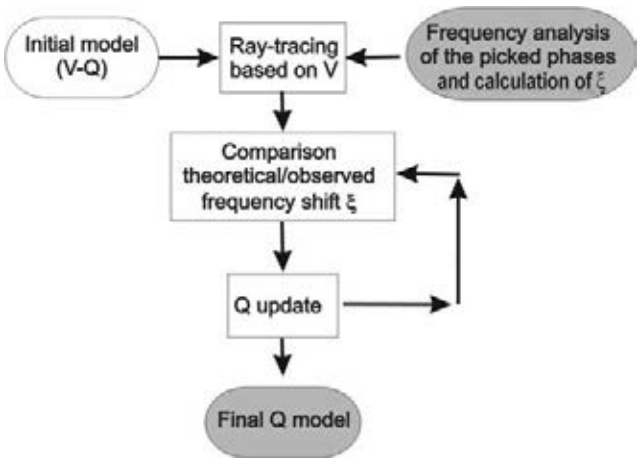

Figure 1 Scheme of the procedure followed in the attenuation tomographic inversion. The initial model consists of the P-wave velocity (V) from the tomographic inversion, and the P-wave quality factor (Q), which is constant as a first guess. The velocity information is used only for the ray tracing, whereas the residuals of the spectral content of the seismic pulses are used to improve the Q-model throughout the tomographic loop.

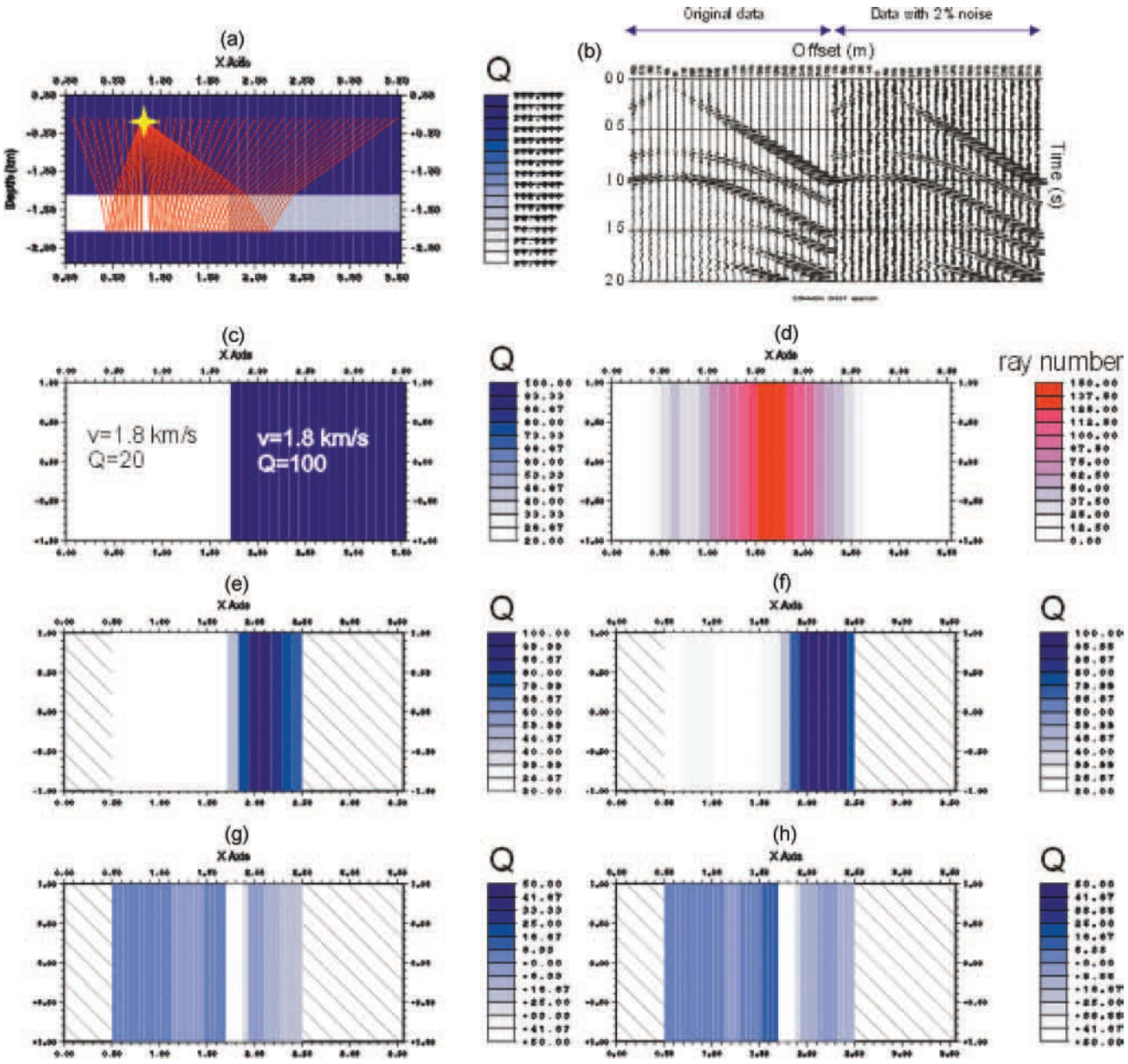

Figure 2 The synthetic model. (a) Vertical section: the quality factor (Q) of the various layers is indicated. The yellow star indicates the source, and some rays are traced (thin red lines). (b) Shot gather, from the seismic modelling (left), and with 2% added noise (right). (c) Planar view of the attenuating intermediate layer: the velocity (v) and quality factor (Q) values are indicated. (d) Ray number in the tomographic model. (e) Q results of the inversion (noise-free data); the parts of the model that are poorly covered by the rays are masked. (f) Q results of the inversion (noisy data); the parts of the model that are poorly covered by the rays are masked. (g) Q-residuals from the noise-free data inversion. (h) Q-residuals from the noisy data inversion.

obtaining a smoothed image that has a higher resolution than the base grid, without the unwanted effect of a poor coverage (Vesnaver and Böhm 2000).

Figure 1 illustrates the whole procedure described above for attenuation inversion. This procedure implies that there is a risk of error propagation from the velocity values, obtained by traveltime tomographic inversion, to the Q-values, calculated by frequency-shift analysis, and that therefore it is important to have a reliable velocity field as a reference (Quan and Harris 1997).

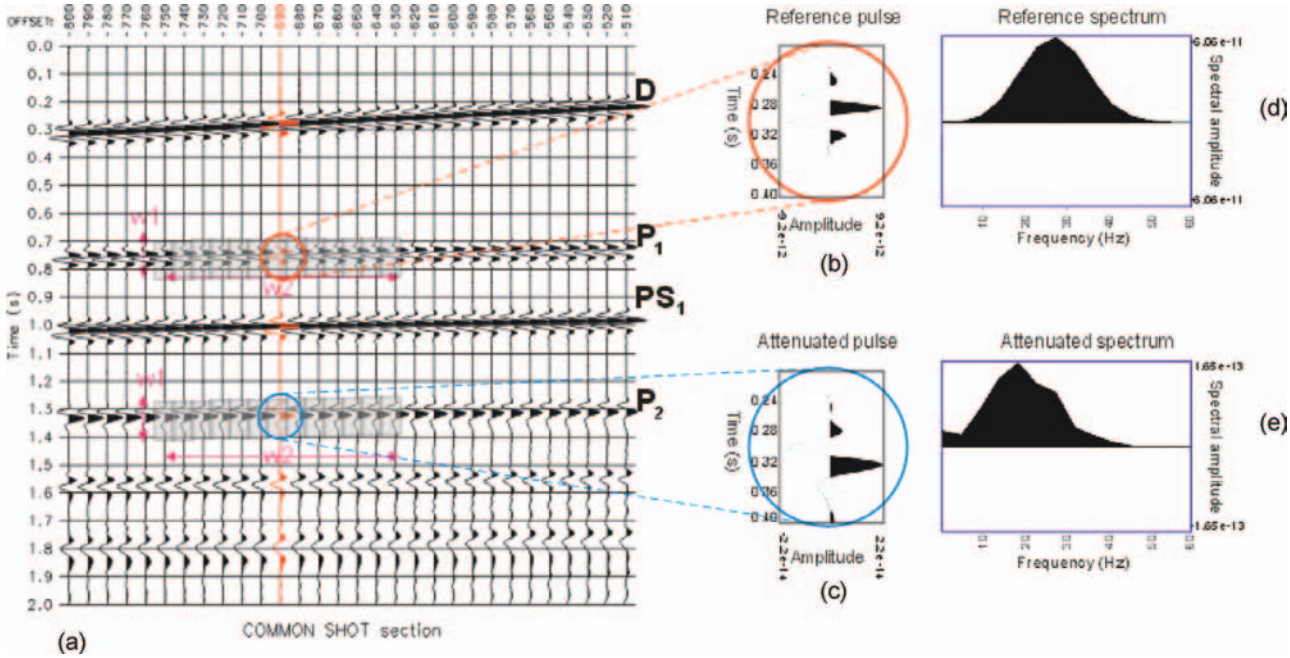

Figure 3 (a) An example of a synthetic shot gather: D = direct arrival, P1 = P-wave reflected from the first interface; PS1 = Converted S-wave from the first interface; P2 = P-wave reflected from the second interface (bottom of the attenuating medium). The grey shading indicates the trace portions considered for the analysis. w1: temporal window over which the spectral analysis is performed; w2: trace window to average the spectra. (b) Reference pulse (P1) and (d) its power spectrum. (c) Pulse P2 and (e) its power spectrum.

A SYNTHETIC EXAMPLE

We first test the algorithm using a synthetic seismogram. Figure 2(a) shows the model, given by a medium where Q varies laterally from 20 to 100 within a medium with infinite Q. The velocity in the intermediate layer is overall 1.8 km/s, while above and below it, the velocity is 3 km/s (Fig. 2c). The numerical mesh to generate the seismograms has 1001 × 468 points, with a grid spacing of 10 m. In order to avoid wraparound, absorbing strips having a width of 50 gridpoints are implemented at the boundaries of the mesh. All the media are isotropic. To compute the synthetic seismograms, we use the time-domain equations for wave propagation in a heterogeneous viscoelastic medium described by Carcione (1995). The anelasticity is described by the standard linear solid, also known as the Zener model (Zener 1948; Ben-Menahem and Singh 1981). The modelling algorithm is based on a 4th-order Runge–Kutta time-integration scheme and on the staggered Fourier method to compute the spatial derivatives (e.g. Carcione and Helle 1999). The source is a dilatational force with the time history of a Ricker wavelet and a dominant frequency of 25 Hz. The source is indicated by a star in Fig. 2(a). Figure 2(b) shows the synthetic seismograms generated (left) and the same records with 2% noise added (right).

The frequency-shift analysis procedure is illustrated in Fig. 3(a), where only some of the traces are shown. Different phases may be recognized: the first arrivals (D); the P-wave reflection from the first interface, i.e. the top of the attenuating medium (P1); the S-wave converted at the same surface (PS1); the P-wave reflection from the second interface, i.e. the bottom of the attenuating layer (P2). A time-window of width *w1* is centred on the traveltimes of the reference event (the reflection from the top of the attenuating layer, P1) and of the event we want to analyse (the reflection from the bottom of the attenuating layer, P2), so as to follow their moveout. The amplitude spectra of the reference pulse (Fig. 3b) and of the attenuated pulse (Fig. 3c) are shown in Fig. 3(d, e). The decrease in pulse amplitude and the loss of high frequencies are evident, both in the wavelet shape and in the spectrum shift toward the low frequencies. To minimize possible noise problems and to make the analysis more robust, a sliding window of some traces (*w2* in Fig. 3a) is used for the analysis. The trace spectra, interpolated with a fifth-order polynomial, are averaged and assigned to the central trace. In this case, a window of 30 traces is used. The effects of the interpolating function on the spectra are shown in Fig. 4(a, b) for the reference pulse and for the attenuated pulses. In the case of the reference pulse, which has a Gaussian spectrum, the spectral centroid

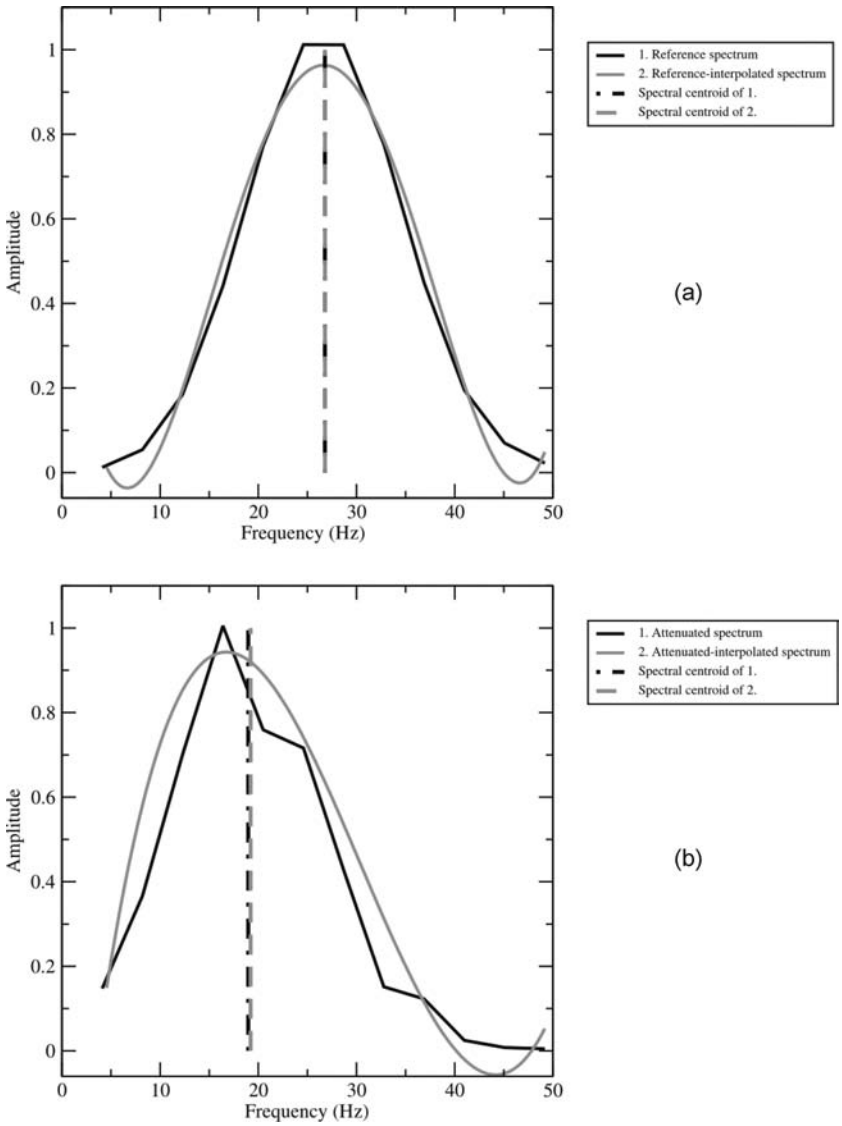

Figure 4 Amplitude spectra of the reference pulse (a) and of the reflection from the bottom of the attenuating layer (b). Black line: original data; grey line: interpolated spectra. The positions of the relative centroids are indicated by a black dashed line and a grey dashed line, respectively for the centroid of the original spectrum and for the centroid of the interpolated spectrum.

coincides with the maximum frequency, and it also coincides with the maximum frequency calculated on the basis of the interpolated spectrum. In contrast, in the case of the attenuated pulse, the spectral centroid is no longer coincident with the spectral maximum amplitude, and there is a very small difference between the spectral centroid calculated on the basis of the original spectrum (18.97 Hz) and the spectral centroid obtained by interpolation (19.22 Hz).

We used the frequency-shift data as input for our attenuation tomography. In this case, we did not invert the velocity field, and therefore our starting model for velocity is the real one. We tested initial Q-values varying from 1 to 999, and obtained very similar results for the areas of the model well covered by the rays, since the ray coverage affects the quality and reliability of the tomographic inversion of the attenuation. The lateral sides of the model are relatively poorly covered by the rays. As expected, the part of the model with $Q = 100$ is covered only in its central part, due to the ray bending (Fig. 2d). We therefore masked the model outside the limits, $x = 0.5$ and $x = 2.5$ (Fig. 2(e–h), because if the ray coverage is poor and the null space energy is high, the values obtained depend too much on the initial model, and are therefore unreliable. However, where the ray coverage is sufficient, the resolution of the Q-factor is good, with an error of about 4%, increasing to 10% across the boundary between the two zones with different Q (Fig. 2e). Figure 2(g) shows the misfit between the inversion results and the real model. The main discrepancy is in the pixel located at about $x = 1.8$, i.e. corresponding to

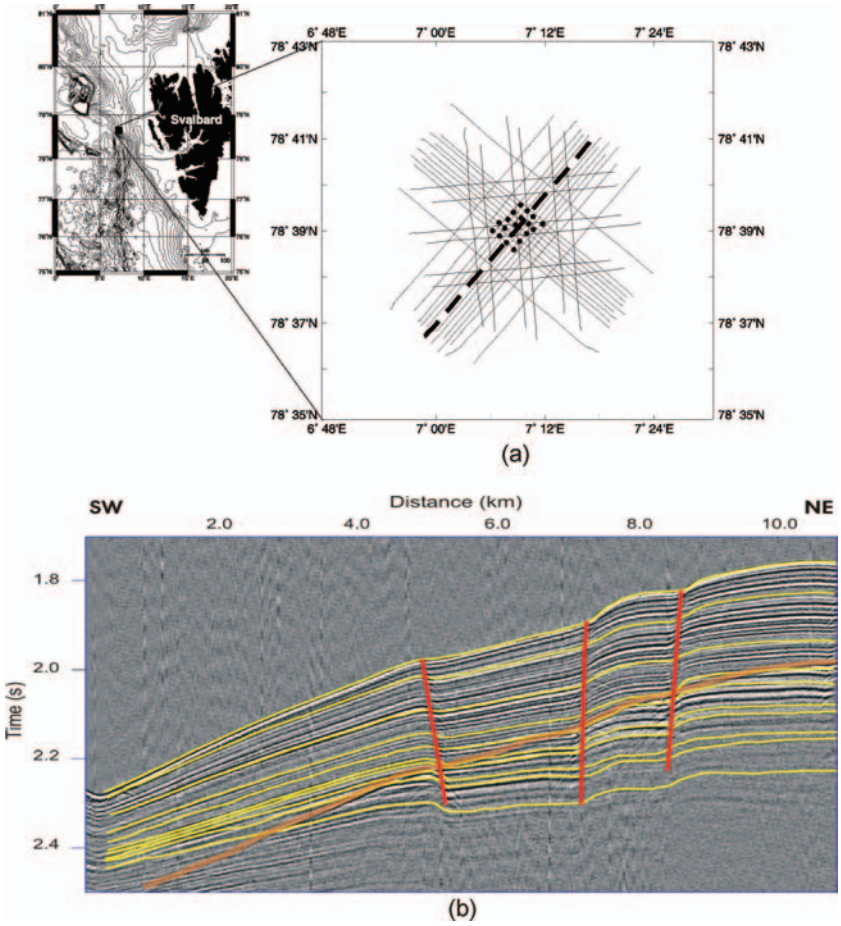

Figure 5 (a) Location map of the seismic lines acquired offshore NW Svalbard during the 2001 Hydratech survey. The dots are the OBSs. The thick dashed line corresponds to shotline 4. (b) Single-channel seismic section from shotline 4. Thick orange line: the bottom-simulating reflector (BSR); red lines: faults; thin yellow lines: picked reflected events.

the contact between $Q = 20$ and $Q = 100$. This is due to the use of the lateral sliding window ($w2$) for the calculation of the spectral centroid shift. When we consider the data set with noise added (Fig. 2f, h), as expected the absolute values show a larger error with respect to the real model (about 6%, increasing to 14% across the boundary), but it appears that this procedure is also sufficiently robust in the presence of noise. Assuming an uncertainty of 3 Hz in the measurements, we obtain chi-squared (χ^2) values for the frequency-shift residuals of 0.44 and 1.35 for the noise-free case and the case with added noise, respectively.

THE REAL CASE

The 3D seismic data of the real data set were acquired within the framework of the European Union Hydratech project, with the aim of identifying the presence of gas hydrate and free gas in the sediments of continental margins and quantifying their amounts. As is well known, the boundary between the gas-hydrate- and free-gas-bearing sediments is marked by a bottom-simulating reflector (BSR), which is sub-parallel to the sea-floor reflection, with opposite polarity. A clear frequency and amplitude variation in the seismic reflectors is observed across the BSR, due to the presence of the free gas beneath it, and data collected in such areas may therefore be suitable for the application of attenuation tomography. The 2001 Hydratech survey took place on the western continental margin of Svalbard, on the lowest part of the continental slope, close to the intersection of the active mid-ocean Knipovich Ridge with the Molloy transform system (Westbrook *et al.* 2005). The acquisition pattern was given by an array of 20 four-component ocean-bottom seismographs (OBSs), spaced at intervals of 400 m. A dense pattern of shotlines, 200 m apart and 10 km long, spanned a wide azimuth interval, having offsets of 5–6 km (Fig. 5a). The frequency bandwidth of the signal recorded is nearly 200 Hz, so as to enable the evaluation of the frequency shift induced by the presence of gas.

The seismic profiles show a well-stratified sequence of reflections down to about 400–500 ms below the seabed (at about 1400 m depth), dipping south-westwards. From the

information of a neighbouring ocean-drilling-program site, the sequence consists of a series of silty clays with minor occurrence of clay with silt, but there is also common occurrence of sandy layers (Forsberg *et al.* 1999). Two sets of antithetic faults related to the Knipovich Ridge and to the Molloy structure respectively, cut across the continental slope, bordering the area where the OBSs were placed (Vanneste, Guidard and Mienert 2005). The BSR is mostly evident on the downslope profiles at about 250 ms below the seabed, showing opposite polarity with respect to the seafloor reflection, and causing a change in amplitude, frequency content and, in some cases, also in the pulse polarity in the crossed reflections of the underlying sedimentary sequence. Figure 5(b) shows a downslope seismic line (shotline 4): the BSR, three faults and the picked reflections are drawn. Ten reflections were chosen for the tomographic analysis (four above the BSR and six below it) (Fig. 5b). We did not consider refracted arrivals and post-critical reflections, because the crossing and consequent interference between these phases may affect the picking of arrival times. An automatic iterative procedure provided both velocity distribution with depth, as well as the depth position and shape of the reflectors, with a layer-stripping-type method (Vesnaver *et al.* 2000). We start our tomographic inversion by employing an initial model, which is composed of a horizontal interface at some arbitrary depth, overlain by a homogeneous medium. The position of the estimated reflection points and their dispersion is used to build up a new interface. A 2D bicubic spline is fitted through the nearest-offset points and becomes the new reflecting interface for the next ray tracing and tomographic inversion. This results in a total of about 60 iterations for each layer. During this phase we used a coarse grid to be sure of a reliable inversion. Once the depth velocity structure and the

Table 1 Root-mean-square traveltime residuals and relative χ^2 for the ten layers of the model, obtained at the end of the traveltime tomographic inversion that provided the 3D depth velocity model. χ^2 is calculated assuming an uncertainty of 6 ms in traveltime picking

Layers	dt_{RMS} (s)	χ^2
1	0.012	1.024
2	0.010	1.051
3	0.009	1.026
4	0.011	1.366
5	0.009	0.788
6	0.014	1.086
7	0.018	1.576
8	0.014	1.137
9	0.016	1.228
10	0.013	1.161

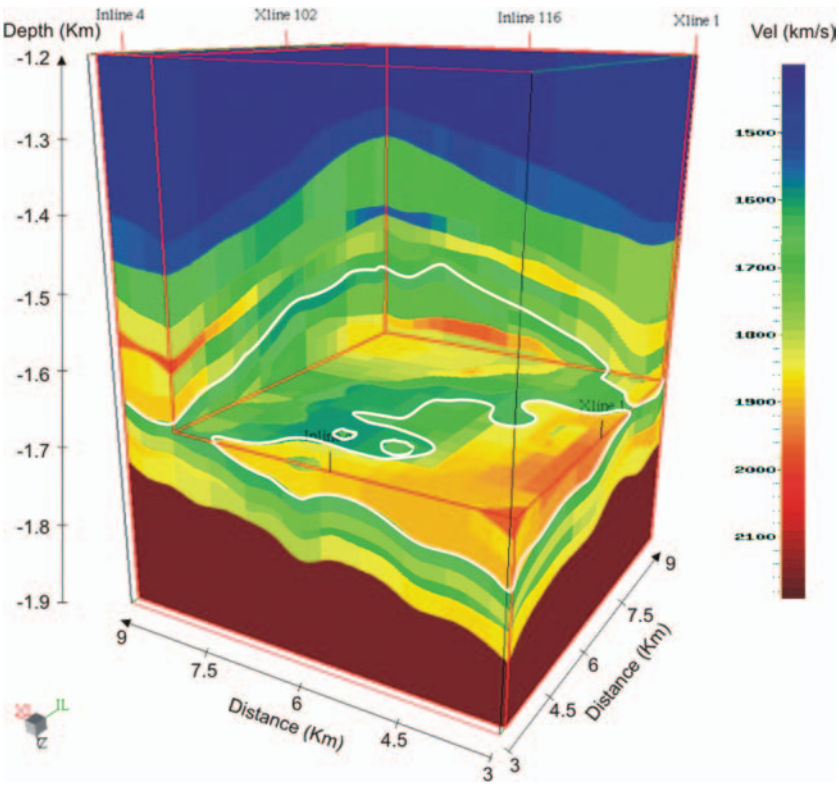

Figure 6 3D velocity tomographic model. The thick white line corresponds to the BSR on the seismic cube.

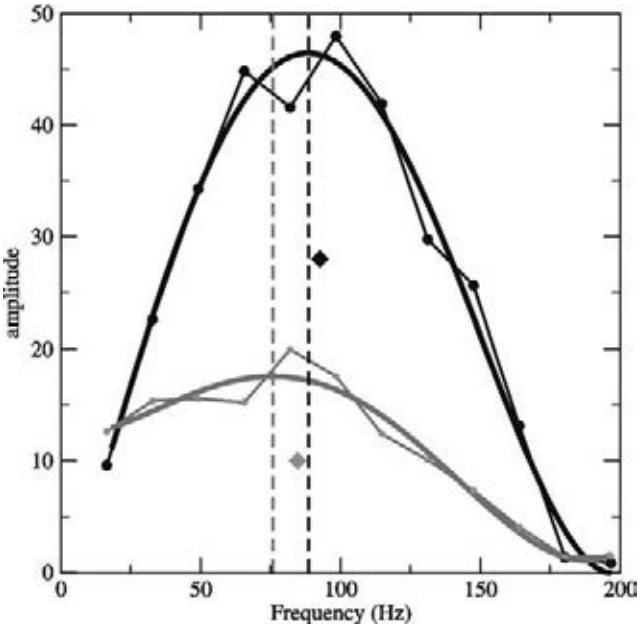

Figure 7 Amplitude spectra corresponding to the reference pulse (thin black line) and to an event below the BSR, i.e. the seventh one (thin grey line). The thick lines are the interpolated spectra, and the two diamonds indicate the locations of the frequency centroids of the two spectra. The dashed black line and the dashed grey line indicate the maximum values for the two spectra.

geometry of the reflectors had been obtained, the staggered-grids procedure was applied by inverting only for the velocity, so to obtain a high-resolution image without loss of reliability. Table 1 shows the root-mean-square residuals for traveltimes obtained for the final model, as well χ^2 for each layer, assuming an uncertainty in our picking of 6 ms, which implies an uncertainty in velocity of about 5–6 m/s and in depth of about 5 m.

The resulting 3D velocity cube in depth has been used by the project partners as follows: (1) as a reference for the more detailed waveform inversion of the records from shotlines parallel to strike at three OBSs, (2) as input for the 3D migration, and (3) to quantify the amount of gas hydrate and free gas within the sediments, through comparison with theoretical models (Westbrook *et al.* 2005; Carcione *et al.* 2005). Confirmation of the validity of the tomographic values is obtained from comparison with the independent 2D ray-tracing-based velocity inversion (Zelt and Smith 1992) performed on dip and cross-lines, and from the final results of the waveform inversion, which both give similar functions of velocity with depth (Westbrook *et al.* 2005).

Figure 6 shows the 3D velocity model obtained by the 3D traveltime inversion (Rossi *et al.* 2004, 2005; Carcione *et al.* 2005; Westbrook *et al.* 2005). Note the interference pattern between the general velocity increase with depth of the sedimentary sequence and the velocity variations due to the presence of gas hydrate and free gas across the BSR (white thick line) within an interval of about 100–150 m thickness. The velocity varies from 1470 to 1760 m/s above the BSR and from 1560 to 1900 m/s below it. The null space energy of the model has been calculated in order to evaluate the reliability of the velocity values. As stated above, this quantity is related not only to the ray number, but also to the angular coverage, linear dependence between the ray equations, and the ray-segment length. On the basis of its value, it is therefore possible to evaluate the reliability of the velocity values obtained throughout the inversion, and consequently to delete the areas where the reliability is too low.

This 3D velocity model is the starting model for the attenuation tomography inversion: the velocity distribution with depth drives the ray tracing, and it is used to convert α to Q. The uncertainty in velocity due to uncertainty in picking implies a maximum uncertainty in Q-values of 1, with an average value of 0.4. An initial value of 40 is used for Q in the whole model. Different values have been tested, and the results are very similar. This value provided the minimal residuals. Lower and upper bounds of $Q = 1$ and of $Q = 9999$, respectively, were used to limit the models. The model values never reached these bounds throughout the inversion.

We chose the first arrivals as reference pulse, after it was established that no refracted events were included, and that the spectrum is unaltered at large offsets with respect with small or zero offsets. We also tested different averaging windows: the differences are small, and the final choice is based on the minimal residuals of the inversion.

Figure 7 shows the spectra of the direct arrivals (black line) and of the seventh reflector (grey line), located below the BSR: the loss of high frequencies in the latter event is evident, causing a noticeable centroid shift toward the left part of the frequency axis. Note that the centroid of each spectrum (diamonds in Fig. 7) differs from its maximum by about 4 Hz for the reference spectrum and by almost 9 Hz for the attenuated event, as shown by the dashed lines in Fig. 7.

The frequency-shift analysis was carried out on the ten reflections used for the traveltime inversion, and we performed the attenuation tomographic inversion using the velocity model of Fig. 6 for the ray tracing. We used fewer lines than for the traveltime inversion, and hence a coarser base grid, to ensure the reliability of the solution. The Q-values vary between 200 and 25, with higher values (150–200) above the BSR and lower values (25–40) below it, as expected. The

Table 2 Root-mean-square residuals of the frequency shift and relative χ^2 for the ten layers of the model, obtained at the end of the frequency-shift tomographic inversion that provided the 3D depth Q-model. χ^2 is calculated assuming an uncertainty of about 5 Hz in our estimate of the shift of the centroid

Layers	$d\xi_{RMS}$	χ^2
1	0.009	0.664
2	0.009	0.84
3	0.010	1.054
4	0.010	1.018
5	0.009	1.159
6	0.010	1.197
7	0.011	1.705
8	0.013	1.25
9	0.013	0.99
10	0.016	1.343

values are compatible with those observed for fine sediments (e.g. Hamilton 1972; Leurer 1997). Table 2 shows the root-mean-square residuals in the frequency shift obtained for the final model, as well χ^2 for each layer, assuming an uncertainty in our estimate of the centroid's shift of about 5 Hz.

Figure 8 shows two vertical sections of the multiparameter model along shotline 4, which is a line that cuts obliquely through the sedimentary wedge. Only the pixels with null space energy of less than 0.4 are shown. Note that the null space energy depends not only on the ray coverage, but also on the layer thickness, and therefore on the lengths of the ray segments; this may lead to artefacts in SIRT inversion (Spakman and Nolet 1988). The difference between the coverage in velocity and Q is due to the coarser grid used in Q-inversion. It is interesting to compare the results of Q-inversion with the seismic data: for this purpose, the near trace line of Fig. 5(b) has been migrated to depth using our tomographic velocity field as input, and it is shown in Fig. 8(c) at the same scale as the velocity and Q-sections. There is a decrease in both velocity and Q across the BSR, due to the presence of free gas; this is demonstrated by a general decrease in the seismic frequencies. The thin layer above the BSR, characterized by a strong increase in Q and a moderate increase in velocity, should also be noted. The velocity variation across the BSR is 150–200 m/s while we observe a Q-variation of about 200. Another feature of the Q-section is that the Q-values decrease upslope. Looking at the seismic data, we can see that, starting from $x = 7$, and therefore to the left of one of the faults bordering our central zone, there is a decrease in the frequency content in some of the shallowest layers, starting from the sea-floor. It must, however, be remembered that our velocity and Q-values are relative to layers thicker that those constituting the sedimentary sequence and the seismic sections, and therefore they necessarily give an averaged image of the velocity and attenuation changes.

To appreciate the lateral variations of both the P-wave velocity and Q, a horizontal slice about 160 m below the sea-bed is shown in Fig. 9(a, b). Figure 9(c) shows the corresponding horizontal section of the null space energy cube. We chose the less favourable section, i.e. the null space energy of the attenuation inversion, performed with a coarser grid. The section related to the velocity is more detailed, and the reliable volume is wider. Note that the slice cuts horizontally through the layers dipping downslope. These layers are characterized by different null space energies, depending on the ray coverage and distribution within them. The central part, where the OBSs are placed, is the area where the null space energy is minimal and we obtain the most reliable results, together with the south-western corner of our model, which is downslope. The projection of the BSR is indicated by a thick pink dashed line, and the fault projections on the horizontal plane are indicated by thick black lines. The high-velocity anomaly due to the possible presence of hydrates has a semicircular shape, and can be correlated with the set of antithetic faults in the centre of the surveyed area. The shape of the area with relatively high Q-values is similar, but there is less continuity with respect to the velocity values. In fact, the Q-values decrease in the south-east corner of the slice, while they increase corresponding to a small fault that is located at the limits of the area where the tomographic inversion is reliable, as shown by the null space energy section (Fig. 9c).

DISCUSSION

In order to discover if some process, other than normal sediment compaction, influences the seismic velocities, we generally refer to some theoretical empirical reference curve for fine-grained sediments, following, for example, Hamilton (1980). Figure 10(a) shows different vertical profiles below four of the OBSs, compared with the Hamilton profile, both as a continuous profile and in terms of interval velocities (thick green lines). For each profile, two dashed lines with the same colour are added to represent the uncertainty of our inversion, both in velocity and Q-values, and in depth. As can be seen, however, the values are small. Above the BSR there is a positive velocity anomaly, while a marked velocity decrease is observed below the BSR within an interval approximately 100–150 m thick. The S-wave velocity in the region through

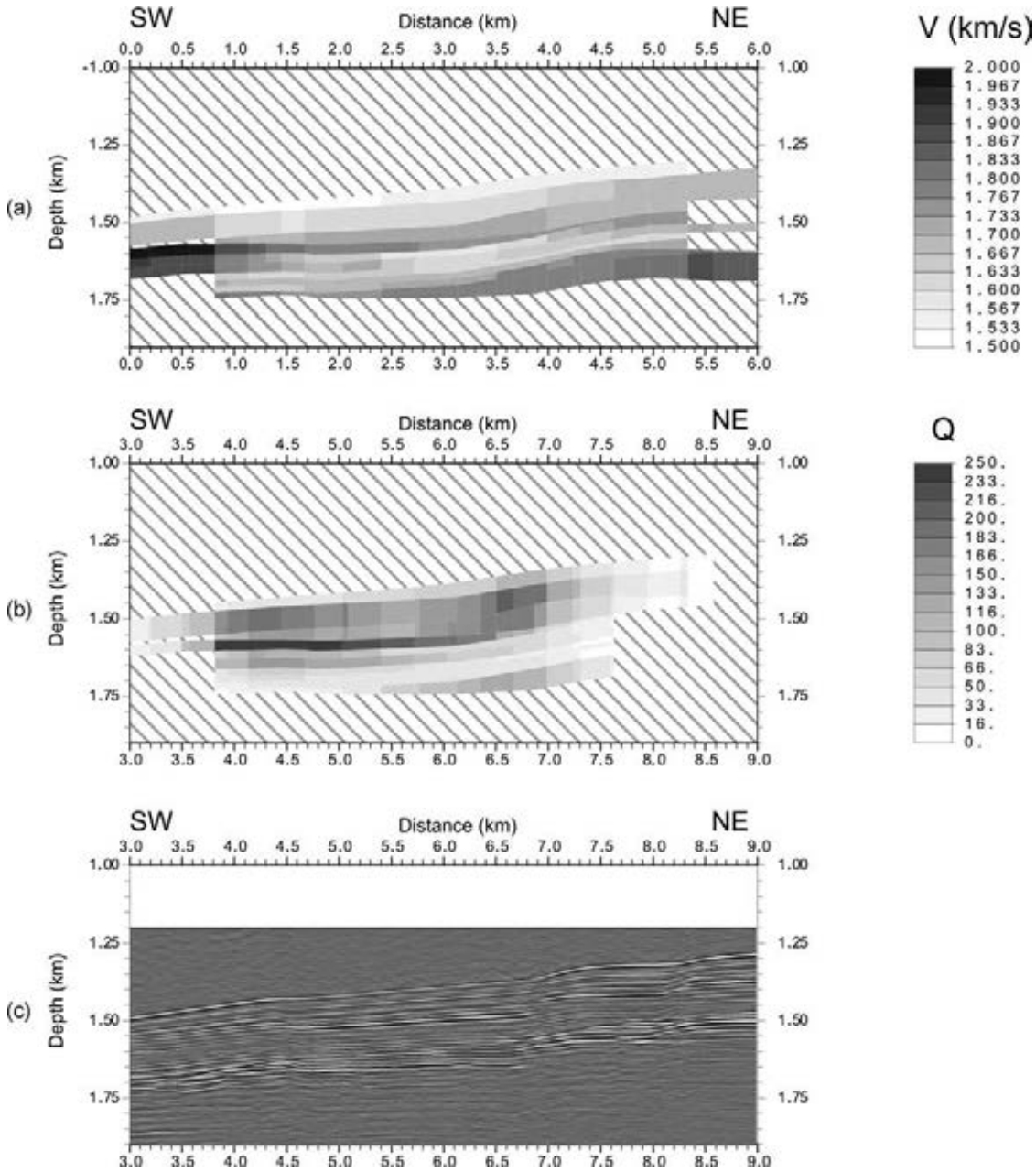

Figure 8 Vertical section of the velocity and quality factor model along shotline 4. (a) P-wave velocities (V); (b) P-wave quality factor (Q). The pixels with null space energy values greater than 0.4 are deleted. (c) Depth-migrated near-trace seismic section of shotline 4.

the BSR shows only small variations from a general increase with depth (Westbrook *et al.* 2005). On this basis, Westbrook *et al.* (2005) concluded that the cause of the pronounced decrease in P-wave velocities beneath the BSR is the presence of free gas, whereas above the BSR, if the hydrate acts to cement grains and increase the shear modulus of the sediment, then the amount of hydrate present is relatively low. An average hydrate concentration of 11% is estimated, whereas beneath the BSR, the free-gas concentration depends strongly on the choice of saturation model: a maximum free-gas saturation of 0.4% is predicted for a uniform-distribution model, and 9% is predicted for a patchy-distribution model (Westbrook *et al.* 2005; Carcione *et al.* 2005).

As stated before, the seismic quality factor may help to determine the presence of pore-fluids and pore-fillings, and to quantify saturation, porosity and permeability (e.g. Wyllie

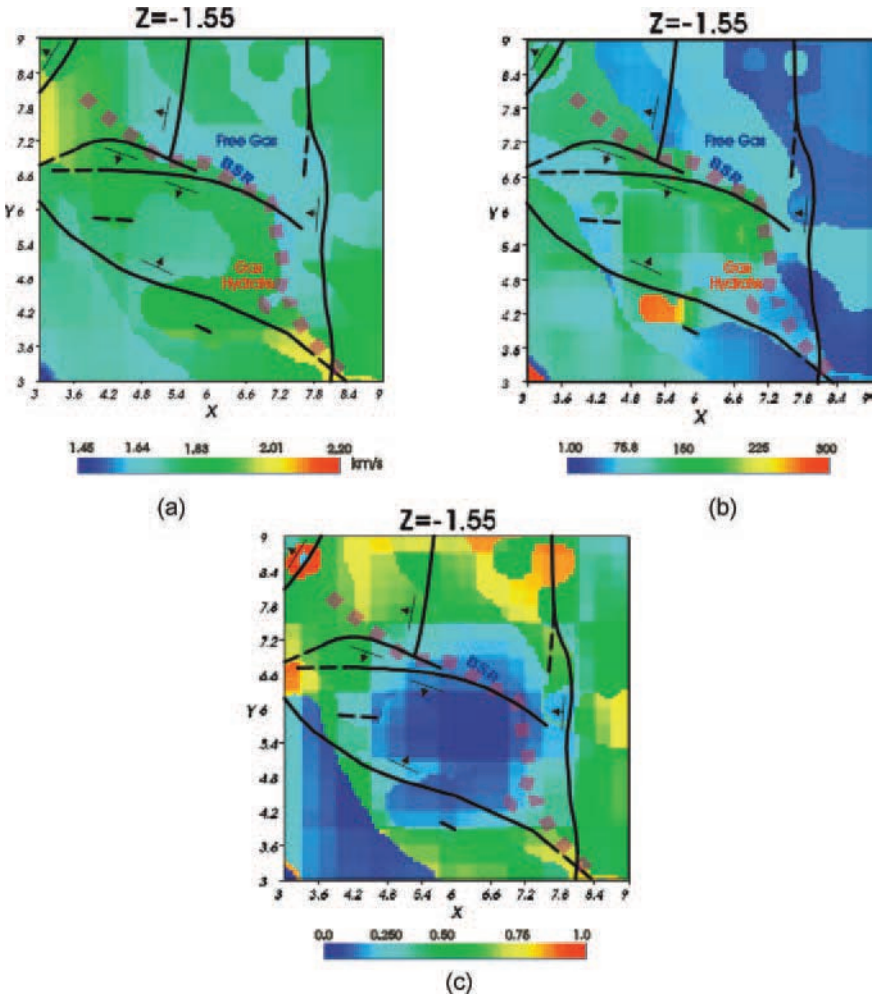

Figure 9 Plane view of the horizontal slice of the velocity and quality-factor model at a depth of 1.55 km (about 150–160 m b.s.f.). (a) Velocity (V), (b) quality factor (Q), (c) null space energy (NSE). Dashed thick pink line: projection of the BSR; black thin lines: projections of the main faults present in the area; arrows: slip direction.

et al. 1962, 1963; Gardner *et al.* 1964; Mavko and Nur 1979; Berryman 1988). In general, we found high Q-values above the BSR, and low values below it. It should be noted that in the shallowest part a greater variation of Q-values, compared with the corresponding velocity variations, is observed, with lower Q-values downslope, possibly due to variations in the instrument coupling or in the shallowest sediments. Across the BSR, the Q-values are more homogeneous: a strong decrease below the BSR is observed, with values compatible with the presence of free gas in the sediments. Above the BSR, where the hydrates are present, Q shows higher values (Figs 8 and 9b) in agreement with the data reported by Wood, Holbrook and Hoskins (2000) and with theories that assume a cementation of the solid frame due to the presence of hydrate (Gei and Carcione 2003), although there is still a debate about the effect of hydrates on seismic-wave attenuation (e.g. Guerin and Goldberg 2002; Chand and Minshull 2004; Chand *et al.* 2004; Priest *et al.* 2006). The same trend can be observed in Fig. 10(b), where anomalous high values of Q above 150 are not characteristic of ocean-bottom fine sediments at 1.6 km depth. In particular, Priest *et al.* (2006), on the basis of a laboratory gas-hydrate resonant-column experiment, stated that both P- and S-wave attenuations are highly sensitive to small quantities of hydrate, with a peak between 3 and 5% saturation. For higher saturation, there is an attenuation decrease. Priest *et al.* (2006) suggested that this may be due to cementation of grain contacts, leading to an increase in low aspect-ratio cracks between the hydrate and sand-grains. The full encasement of the grains at higher hydrate saturation reduces the potential fluid-flow into the pore-space, and reduces the

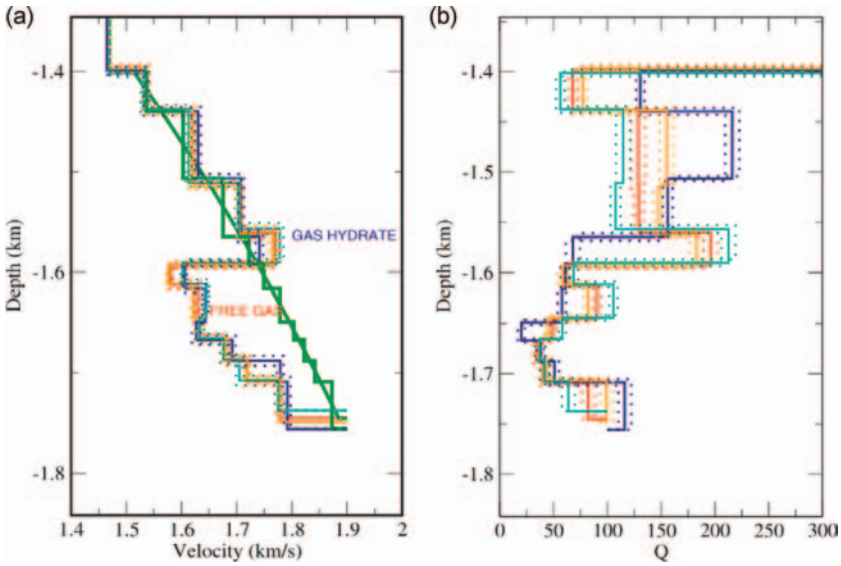

Figure 10 (a) Vertical P-wave velocity profiles and (b) quality-factor profiles below four OBS stations (continuous lines). Dashed lines: the same profiles, with the uncertainty in velocity, depth and *Q*-factor taken into account. The thick green lines in the velocity profiles are reference curves from Hamilton (1980), shown as a continuous function and as interval velocity for the same depth intervals as in our analysis.

attenuation. The gas-hydrate saturation values hypothesized in the Svalbard area are higher than 3–5%, being on average 11% (Carcione *et al.* 2005), which may explain the high values we have found above the BSR. Furthermore, the resonant-column experiment was performed on sands, whereas in our case only some sandy layers should be present in a silty clay sequence (Forsberg *et al.* 1999). The behaviour of these kinds of sediment may be very different from that observed for sands (e.g. Leurer 1997). A similar analysis, carried out in the same area but not in the gas-hydrates stability zone, could give the values of velocity and *Q* for the hydrate-free sedimentary series, for use as a reference.

Note the apparent correlation between both the P-wave velocity and *Q* and the faults present in the area, in particular, the antithetic faults creating a small graben in the centre of the surveyed area (Fig. 9). The faults locally deform the strata, including the sea-bed, and hence affect the subsurface distribution of the temperature, which controls the depth of the BSR. They may also act as fluid-flow pathways, producing localized thermal anomalies and affecting the distribution of hydrate and free gas within the sedimentary sequence. The low *Q*-values observed upslope in the vertical section in Fig. 8(b), within a block limited by two direct faults, may be related to varied temperature conditions and to fluid content.

CONCLUSIONS

We successfully tested the reflection-tomography algorithm for the estimation of the attenuation in sediments, using a synthetic seismogram and a real seismic data set. In particular, we applied the method to the detection of free gas and of gas hydrates within the sediments. The good agreement between P-wave velocity and *Q* variations, with lower values in the free-gas saturated zone and higher values in the gas-hydrate bearing zone, show an apparent correlation with the fault pattern observed in the area. While P-wave velocity shows a positive anomaly above the BSR, when compared with the Hamilton curve, which describes a velocity increases with depth due to sediment compaction, the interpretation of the *Q*-values is more complicated. The observed values are included in the wide range of values reported in the literature for fine-grained sediments. However, without having direct measurements of attenuation in hydrate-free sediments at our disposal, we cannot definitely conclude that the cementation of the grains due to the presence of gas hydrate decreases the attenuation, although this appears to be the case in this study.

ACKNOWLEDGEMENTS

We thank the Hydratech consortium (EC FP5 contract. no. EVK3-CT-2000-00043) for their valuable contribution to the data acquisition and OBS data processing. We are also grateful to Graham Westbrook, Angelo Camerlenghi, Flavio Accaino, Umberta Tinivella and Stefano Picotti for constructive discussions and suggestions. We thank Mirko van der Baan and an anonymous reviewer for the constructive suggestions that helped us to improve the manuscript.

REFERENCES

van der Baan M. 2002. Constant *Q* and a fractal, stratified Earth. *Pure and Applied Geophysics* **159**, 1707–1718.

Ben-Menahem A. and Singh S.G. 1981. Seismic Waves and Sources. Springer Verlag, Inc.

Berryman J.G. 1988. Seismic wave attenuation in fluid-saturated porous media. *Journal of Pure and Applied Geophysics* **128**, 423–432.

Best A.I., McCann C. and Sothcott J. 1994. The relationships between the velocities, attenuations and petrophysical properties of reservoir sedimentary rocks. *Geophysical Prospecting* **42**, 151–178.

Böhm G., Accaino F., Rossi G. and Tinivella U. 2006. Tomographic joint inversion of first arrivals in a real case from Saudi Arabia. *Geophysical Prospecting* **54**, 721–730.

Böhm G., Rossi G. and Vesnaver A. 1999. Minimum time ray-tracing for 3-D irregular grids. *Journal of Seismic Exploration* **8**, 117–131.

Brzostowski M. and McMechan G. 1992. 3-D tomographic images of near surface seismic velocity and attenuation. *Geophysics* **57**, 396–403.

Carcione J.M. 1995. Constitutive model and wave equations for linear, viscoelastic, anisotropic media. *Geophysics* **60**, 537–548.

Carcione J.M. 2001. *Wave Fields in Real Media. Theory and Numerical Simulation of Wave Propagation in Anisotropic, Anelastic and Porous Media*. Pergamon Press, Inc.

Carcione J.M., Gei D., Rossi G. and Madrussani G. 2005. Estimation of gas-hydrate concentration and free-gas saturation at the Norwegian-Svalbard continental margin. *Geophysical Prospecting* **53**, 803–810.

Carcione J.M. and Helle H.B. 1999. Numerical solution of the poro-viscoelastic wave equation on a staggered mesh. *Journal of Computional Physics* **154**(2), 520–527.

Carcione J.M., Helle H.B. and Pham N.H. 2003. White's model for wave propagation in partially saturated rocks: Comparison with poroelastic numerical experiments. *Geophysics* **68**, 1389–1398.

Carcione J.M., Helle H. and Zhao T. 1998. The effects of attenuation and anisotropy on reflection amplitude versus offset. *Geophysics* **63**, 1652–1658.

Carcione J.M. and Picotti S. 2006. P-wave seismic attenuation by slow-wave diffusion. Effects of inhomogeneous rock properties. *Geophysics* **71**, 1–8.

Chand S. and Minshull T.A. 2004. The effect of hydrate content on seismic attenuation: A case study for Mallik 2L-38 well data, Mackenzie delta, Canada. *Geophysical Research Letters* **31**, L14609.

Chand S., Minshull T.A., Gei D. and Carcione J.M. 2004. Gas hydrate quantification through effective medium theories – a comparison. *Geophysical Journal International* **159**, 573–590.

Chapman M., Liu E. and Li X.-L. 2006. The influence of fluid-sensitive dispersion and attenuation on AVO analysis. *Geophysical Journal International* **167**, 89–105.

Dasgupta R. and Clark R.A. 1998. Estimation of *Q* from surface seismic reflection data. *Geophysics* **63**, 2120–2128.

Dobroka M., Dresen L., Gelbke C. and Rüter H. 1992. Tomographic inversion of normalized data: double trace tomography algorithms. *Geophysical Prospecting* **40**, 1–14.

Forsberg C.F., Solheim A., Elverøi A., Jansen E., Channel J.E.T. and Andersen E.S. 1999. The depositional environment of the western Svalbard margin during the late Pliocene and the Pleistocene: sedimentary facies changes at site 986. In: *Proceedings of ODP, Scientific Results, 162* (eds M.E. Raymo, E. Jansen, P. Blum and T.D. Herbert): College Station, TX (Ocean Drilling Program).

Gardner G.H.F., Wyllie M.R.J. and Droshak D.M. 1964. Effects of pressure and fluid saturation on the attenuation of elastic waves in sands. *Journal of Petroleum Technology* 189–198.

Gei D. and Carcione J.M. 2003. Acoustic properties of sediments saturated with gas hydrate, free gas and water. *Geophysical Prospecting* **51**, 141–157.

Guerin G. and Goldberg D. 2002. Sonic waveform attenuation in gas hydrate-bearing sediments from the JAPEX/JNOC/GSC Mallik 2L-38 research well, Mackenzie Delta, Canada. *Journal of Geophysical Research* **107**, 10.1029/2001JB000556.

Hamilton E.L. 1972. Compressional-wave attenuation in marine sediments. *Geophysics* **37**, 620–646.

Hamilton E.L. 1980. Geoacoustic modelling of the sea-floor. *Journal of the Acoustical Society of America* **68**, 1313–1340.

Kjartansson E. 1979. Constant *Q*-wave propagation and attenuation. *Journal of Geophysical Research* **84**, 4137–4748.

Konofagou E.E., Varghese T., Ophir J. and Alam S.K. 1999. Power spectral strain estimators in elastography. *Ultrasound in Medicine and Biology* **25**, 1115–1129.

Leurer K.C. 1997. Attenuation in fine-grained marine sediments: extension of the Biot-Stoll model by the 'effective grain model' (EGM). *Geophysics* **62**, 1465–1479.

Liu L., Lane J.W. and Quan Y. 1998. Radar attenuation tomography using the centroid frequency downshift method. *Journal of Applied Geophysics* **40**, 105–116.

Mavko G.M. and Nur A. 1979. Wave attenuation in partially saturated rocks. *Geophysics* **44**, 161–178.

Picotti S. and Carcione J. 2006. Estimating seismic attenuation (Q) in presence of random noise. *Journal of Seismic Exploration* **15**, 165–181.

Plessix R.E. 2006. Estimation of velocity and attenuation coefficient maps from crosswell seismic data. *Geophysics* **71**, S235–S240.

Priest J.A., Best A.I. and Clayton C.R.I. 2006. Attenuation of seismic waves in methane gas hydrate-bearing sand. *Geophysical Journal International* **164**, 149–159.

Quan Y. and Harris J.M. 1997. Seismic attenuation tomography using the frequency shift method. *Geophysics* **62**, 895–905.

Rossi G., Madrussani G., Böhm G. and Camerlenghi A. 2004. Tomographic inversion of OBS data, offshore Svalbard Islands. 66th EAGE Conference, Paris, France, Extended Abstracts, P-218.

Rossi G., Madrussani G., Gei D., Böhm G. and Camerlenghi A. 2005. Velocity and attenuation 3D tomography for gas-hydrates studies: the NW offshore Svalbard case. *Proceedings of the 5th ICGH*, Trondheim, Norway, Paper 2040, pp. 677–682.

Roth E.G., Wiens D.A., Dorman L.M., Hildebrand J. and Webb S.C. 1999. Seismic attenuation tomography of the Tonga-Fiji region using phase pair methods. *Journal of Geophysical Research* **104**, 4795–4809.

van der Sluis A. and van der Vorst H.A. 1987. Numerical solution of large sparse linear algebraic systems arising from tomographic problems. In: *Seismic Tomogrophy* (ed. G. Nolet), pp. 49–83. Reidel Publishing Co., Dordrecht.

Spakman W. and Nolet G. 1988. Imaging algorithms, accuracy and resolution in delay time tomography. In: *Mathematical Geophysics*

(eds N.J. Vlaar, G. Nolet, M.J.R. Wortel and S.A.P.L. Cloetingh), pp.155–187. D. Reidel Publishing Co.

Vanneste M., Guidard S. and Mienert J. 2005. Arctic gas hydrate provinces along the western Svalbard continental margin. In: *Onshore-Offshore Relationships on the North Atlantic Margin* (eds B.T.G. Wandås, E. Eide, F. Gradstein and J.P. Nystuen), pp. 271–284. Norwegian Petroleum Society (NPF), Special Publication. Elsevier Science Publishing Co.

Vesnaver A. 1994. Towards the uniqueness of tomographic inversion solutions. *Journal of Seismic Exploration* **3**, 323–334.

Vesnaver A. and Böhm G. 2000. Staggered or adapted grids for seismic tomography? *The Leading Edge* **19**, 944–950.

Vesnaver A., Böhm G., Madrussani G., Petersen S. and Rossi G. 1999. Tomographic imaging by reflected and refracted arrivals at the North Sea. *Geophysics* **64**, 1852–1862.

Vesnaver A. Böhm G. Madrussani G., Rossi G. and Granser H. 2000. Depth imaging and velocity calibration by 3D adaptive tomography. *First Break* **18**, 303–312.

Westbrook G.K., Buenz S., Camerlenghi A., Carcione J.M., Chand S., Dean S., Foucher J.-P., Flueh E., Gei D., Haacke R., Klingenhoefer F., Long C., Madrussani G., Mienert J., Minshull T.A., Nouzé H., Peacock S., Rossi G., Roux E., Reston T., Vanneste M. and Zillmer M. 2005. Measurements of P- and S- wave velocities, and the estimation of hydrate concentration at sites in the continental margin of Svalbard and the Storegga region of Norway. *Proceedings of the 5th ICGH*, Trondheim, Norway, Paper 3004, pp. 726–735.

Wood W.T., Holbrook W.S. and Hoskins H. 2000. In situ measurements of P-wave attenuation in the methane hydrate and gas bearing sediments of the Blake Ridge. In: *Proceedings of ODP, Scientific Results, 164* (eds C.K. Paull, R. Matsumoto and P. Wallace) College Station, TX (Ocean Drilling Program).

Wyllie M.R.J., Gardner H.F. and Gregory A.R. 1962. Studies of elastic wave attenuation in porous media. *Geophysics* **27**, 569–589.

Wyllie M.R.J., Gardner H.F. and Gregory A.R. 1963. Addendum to "Studies of elastic wave attenuation in porous media" by M.R.J. Wyllie, G.H.F. Gardner, and A.R. Gregory (Geophysics, 27, 569–589), *Geophysics* **28**, 1074.

Zelt C.A. and Smith R.B. 1992. Seismic traveltime inversion for a 2-D crustal velocity structure. *Geophysical Journal International* **108**, 16–34.

Zener C. 1948. Elasticity and Inelasticity of Metals. University of Chicago Press.

Zucca J.J., Hutchings L.J. and Kasameyer P.W. 1994. Seismic velocity and attenuation structure of the geysers geothermal field, California. *Geothermics* **23**, 111–126.